Supporting Information

In-situ Construction of Hierarchical TiO_2/Ti_3C_2 Hybrid via Water Steam Etching for High-Performance Potassium-Ion Batteries

Tengfei Li, [a] Lu Wang, [*b] Junwen Duan, [a] Zifeng Liu, [a] Dan Zhou, [a] Chang Xue, [*c] Zhubing Xiao[*a]

[a] Henan Key Laboratory of Photovoltaic Materials, Henan University, Kaifeng 475004, China

Email: zbxiao@vip.henu.edu.cn

[b] Key Laboratory for Liquid-Solid Structural Evolution & Processing of Materials (Ministry of Education), School of Materials Science and Engineering, Shandong University, Jinan 250061, P. R. China.

E-mail: luw2018@163.com

[c] Wenzhou Key Laboratory of Cancer Pathogenesis and Translation, Key Laboratory of Laboratory Medicine, Ministry of Education, School of Laboratory Medicine and Life Sciences, Wenzhou Medical University, 325000, P. R. China.

E-mail: xuechang1989@163.com

Content

Figure S13. The magnified GITT profiles at process of (a) discharging and (b) charging. Schematic illustration of a typical single GITT step *vs.* time during (c) discharging and (d) charging.

Figure S14. (a) The Nyquist plots and (b) Extracted |Z| versus $\omega^{-1/2}$ plots in the Warburg region for TiO_2, Ti_3C_2 and TiO_2/Ti_3C_2 electrodes.

Figure S15. GITT profiles of TiO_2, Ti_3C_2 and TiO_2/Ti_3C_2 electrodes during potassiation/de-potassiation processes.

Figure S16. (a) Rate performance (b) Cycling stability at 0.2 A g^{-1} and (c) Long-term cycling performance at 2 A g^{-1} for Ti_3C_2 and TiO_2/Ti_3C_2 anodes at 300 ℃, 400 ℃ and 500 ℃.

Figure S17. Nyquist plots of Ti_3C_2 and TiO_2/Ti_3C_2 electrodes at 300 ℃, 400 ℃, 500 ℃.

Figure S18. The XRD pattern of the potassium bis (fluorosulfonyl) imide (KFSI)

Figure S19. Calculated charge density differences for a single K adsorbed on the $Ti_3C_2F_2$ The yellow and blue colors represent charge accumulation and charge depletion, respectively.

Figure S20. Cross-sectional SEM images of pristine, after-discharge, and after-charge of the initial cycle for TiO_2/Ti_3C_2 and Ti_3C_2 electrodes.

Figure S21. (a-d) SEM images of electrodes with their SEI after 400 and 2000 cycles for TiO_2/Ti_3C_2 and Ti_3C_2.

Table S1. Atomic percent summary of main elements obtained by XPS survey spectrum analysis for the Ti_3C_2 and TiO_2/Ti_3C_2 hybrid.

Table S2. Summary of previously reported Ti_3C_2-based anode materials for alkali metal ion batteries application, and electrochemical performance.

Reference

Material characterization

The crystalline phases of samples were examined by powder X ray diffraction (XRD) (D8 ADVANCE X-Ray Diffractometer from Bruker Co. Ltd, Germany) using a Cu K_α source at a scanning speed of 10° min^{-1} Morphologies and structures were characterized by field-emission scanning electron microscopy (FESEM, JEOL-7001F, 15 kV), transmission electron microscopy (TEM), high-resolution TEM (HRTEM), and selected area electron diffraction (SAED) (JEOL JEM-2100 system operating at 200 kV). Chemical compositions of the samples were detected with X-ray photoelectron spectroscopy (XPS), (AXIS ULTRA DLD from British Kratos Co. Ltd) using an Al Kα monochromatic X-ray source (1486.6 eV). Raman spectra of the products were conducted with Raman spectroscope (Renishaw in VIA, excited by 514.5 nm laser). Thermal stability of the samples was assessed by thermal gravimetric analysis (TGA) (TAG2) in O_2 atmosphere with a temperature range from 25 to 1000 °C at a heating rate of 5 °C min^{-1}. The specific surface area and pore size distribution of samples were tested using the Tristar II Specific Surface Area Tester based on Brunauer-Emmett-Teller (BET), Barrett-Joyner-Halenda (BJH) and Horvath-Kawazoe (HK) methods.

Electrochemical tests

The electrochemical tests were carried out in coin-cell configurations (CR2032) at room temperature. The working electrodes of TiO_2/Ti_3C_2 and Ti_3C_2 cells were prepared by mixing active materials (70 wt %), super P (20 wt%), and polyvinylidene fluoride (PVDF, 10 wt %) in N-methyl-2-pyrrolidinone (NMP). Copper foil was employed as the current collector and dried under vacuum drying at 60 °C for 12 h, then the electrodes were punched into discs with diameter of 14 mm. Fresh potassium foils were used as counter and reference electrodes, and Whatman glass microfiber filters (GF/F) were used as the separators. The electrolyte was 3.0 M potassium bis (fluorosulfonyl) imide (KFSI) in DME. The coin cells were assembled in an Ar-filled glove box ($O_2 \leq 0.1$ ppm, $H_2O \leq 0.1$ ppm). Galvanostatic discharge/charge measurements were conducted on a LAND CT3001A battery testing system in the potential window of 0.01-3.0 V. Cyclic voltammetry (CV) was conducted using a CHI 660D electrochemical workstation at different scan rates within a voltage window of 0.01-3.0 V. Electrochemical impedance spectroscopy (EIS) was

applied to the cells in the range from 1000 kHz to 0.01 Hz with an amplitude of 5 mV. Galvanostatic intermittent titrations (GITT) were carried out on a Land CT3001A battery testing system. For the pouch full cell assembly, the TiO_2/Ti_3C_2 anode and PTCDA cathode were cut into 4 cm × 6 cm. Thereinto, PTCDA was prepared by annealing at 450 °C for 4 h under Ar atmosphere with a heating rate of 5 °C min^{-1} to improve the conductivity and the PTCDA cathode was prepared in the same way as the TiO_2/Ti_3C_2 anode. Then, both the electrodes were respectively put into the commercial soft Al plastic films using home-made potassium foil as the counter electrode. Meanwhile, the nickel tab and the aluminum tab were connected with the home-made potassium foil and the electrode, respectively. Both anode and cathode were pre-potassiation for 5 cycles at a current density of 50 mA g^{-1} in the commercial soft Al plastic films. Finally, the TiO_2/Ti_3C_2 anode, PTCDA cathode and separators were reassembled in the argon-filled glove box, followed by the injection of electrolyte and the vacuum sealing. Thereinto, the NP ratio is 1.2 and the voltage windows of full cells are 0.5-3.3 V.

Computational Section

Electronic structure calculations were performed with the density functional theory as implemented in the Vienna ab initio simulation package,[1, 2] employing the projected augmented wave potentials to describe the atomic core electrons and the plane wave basis set to expand the Kohn-Sham electronic states.[3] For the exchange and correlation functional, the generalized gradient approximation (GGA) in the Perdew-Burke-Ernzerhof (PBE) format was used.[4] The kinetic energy cutoff was set to 550 eV and the Gamma centered method was employed for the Brillouin zone sampling for all calculations in this work. For all bulk structures, the convergence criteria energy for geometric optimization was 10-5 eV/atom and all the atoms were fully relaxed until the atomic forces are less than 0.02 eV $Å^{-1}$. The $Ti_3C_2O_2$-K model was constructed by the 3×3 supercell. The TiO_2-K model was constructed by the 3×3 supercell. The $Ti_3C_2F_2$-K model was constructed by the 3×3 supercell. The adsorption energy (E_a) is calculated as: $Ea = (E_{TiO2–K} – E_{TiO2}–E_K)$, where, $E_{Ti3C2O2-K}$, $E_{Ti3C2F2-K}$ and E_K represent the DFT energies of the K^+ adsorbed TiO_2, the pure TiO_2 and the K atom in the bulk phase, respectively. The charge transfer of all structures was assessed by the Bader charge analysis.[5]

In addition, to consider the van der Waals interactions, the DFT-D3 method with Becke-Jonson damping was used for all the calculations. The visualizations of the crystal structure and the charge density were by virtue of the VESTA code.[6]

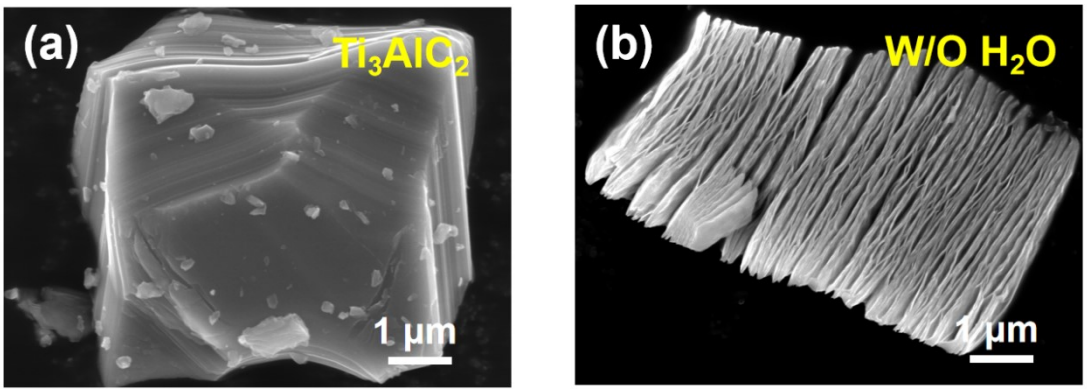

Figure S1. SEM images of bulk Ti_3AlC_2 (a) and Ti_3C_2 without water steam at 800 °C for 5 min (b).

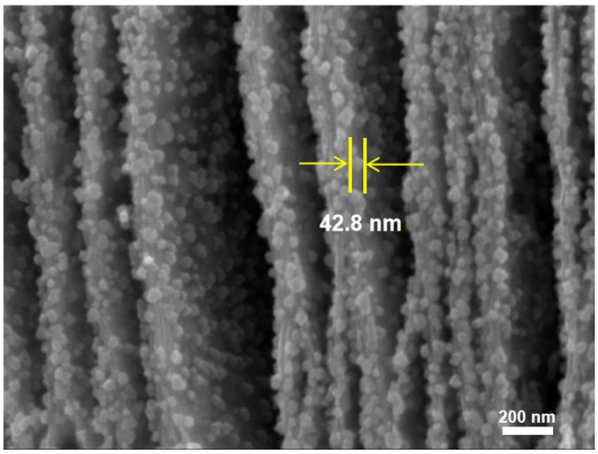

Figure S2. SEM image of TiO_2/Ti_3C_2 hybrid with water steam at 400 °C for 5 min.

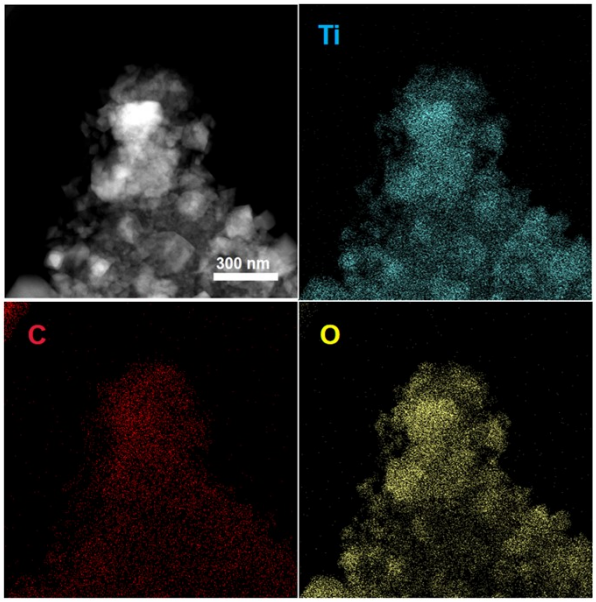

Figure S3. TEM image and corresponding elemental mapping images of TiO_2/Ti_3C_2 hybrid with water steam at 400 °C for 20 min.

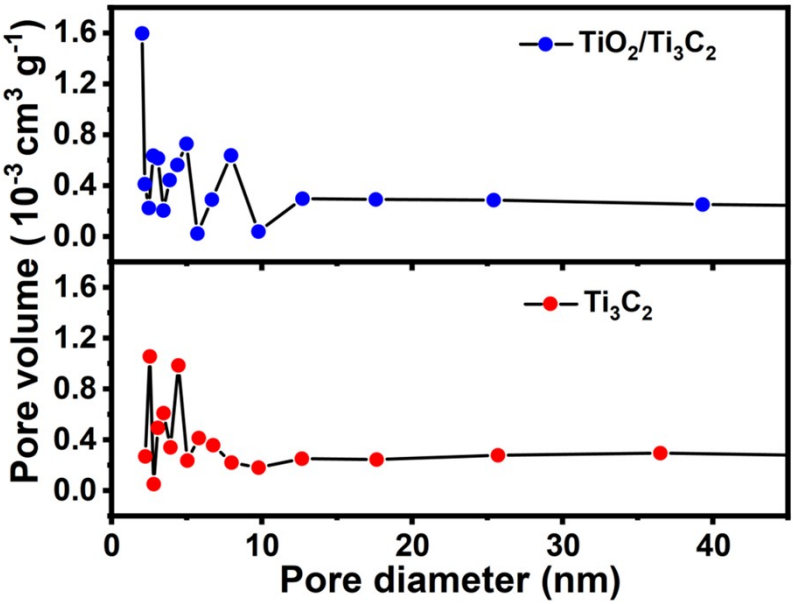

Figure S4. Pore size distributions for the as-prepared Ti_3C_2 and TiO_2/Ti_3C_2 hybrid.

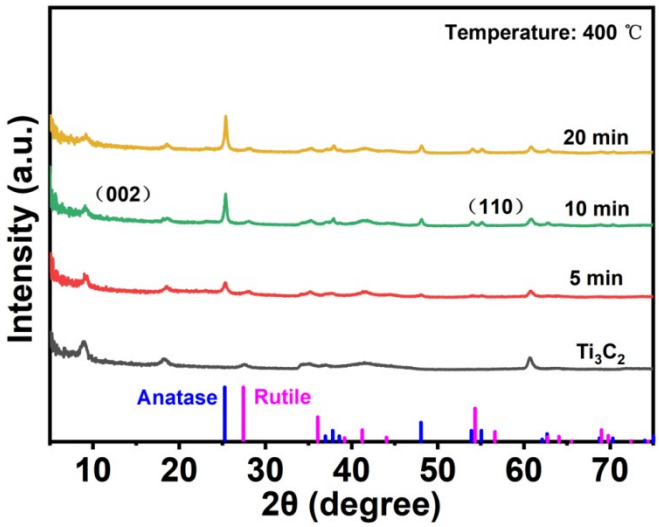

Figure S5. XRD patterns of the Ti_3C_2 and Ti_3C_2-derived samples with water steam at 400 °C for different durations.

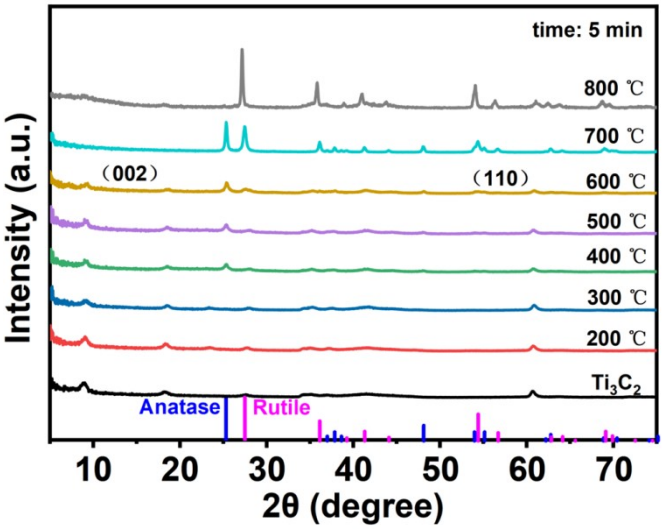

Figure S6. XRD patterns of the Ti_3C_2 and Ti_3C_2-derived samples with water steam for 5 min at different temperature.

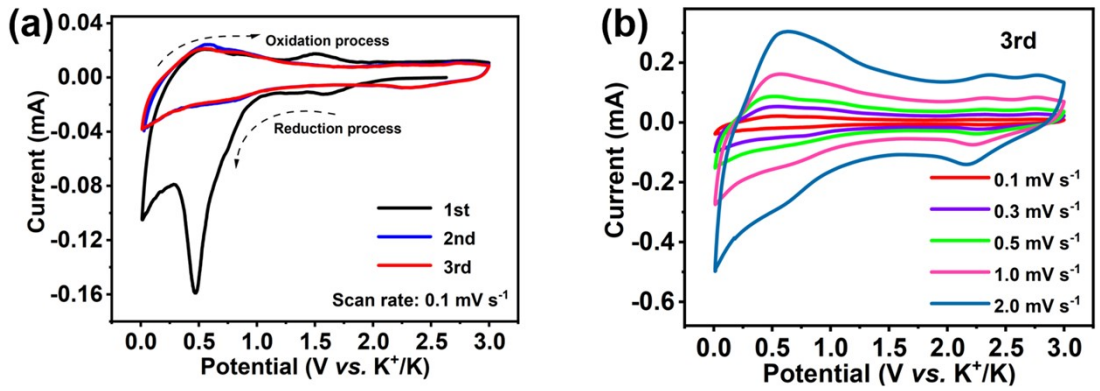

Figure S7. (a) The initial three CV curves at the scan rate of 1 mV s^{-1} and (b) CV curves at various scan rates of Ti_3C_2 anode.

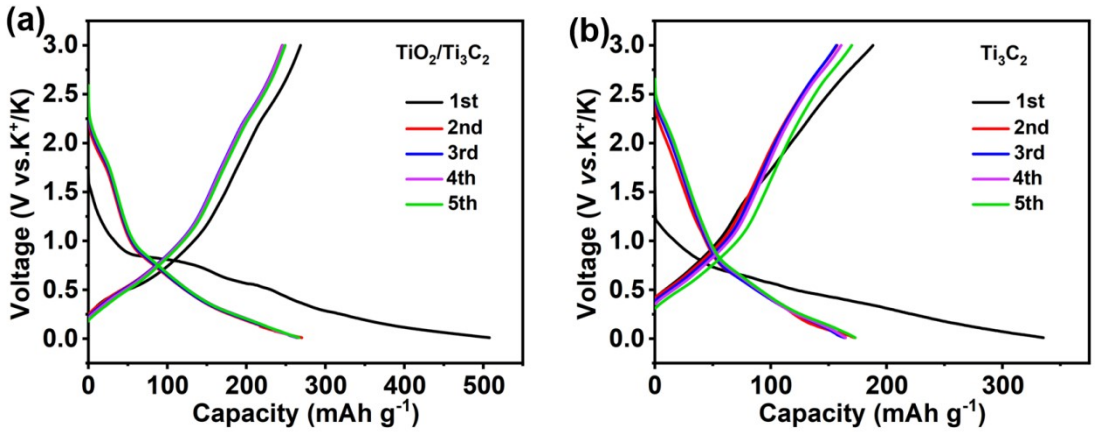

Figure S8. Galvanostatic charge/discharge profiles of the initial five cycles for TiO_2/Ti_3C_2 hybrid (a) and Ti_3C_2 electrode (b) at 0.1 A g^{-1}.

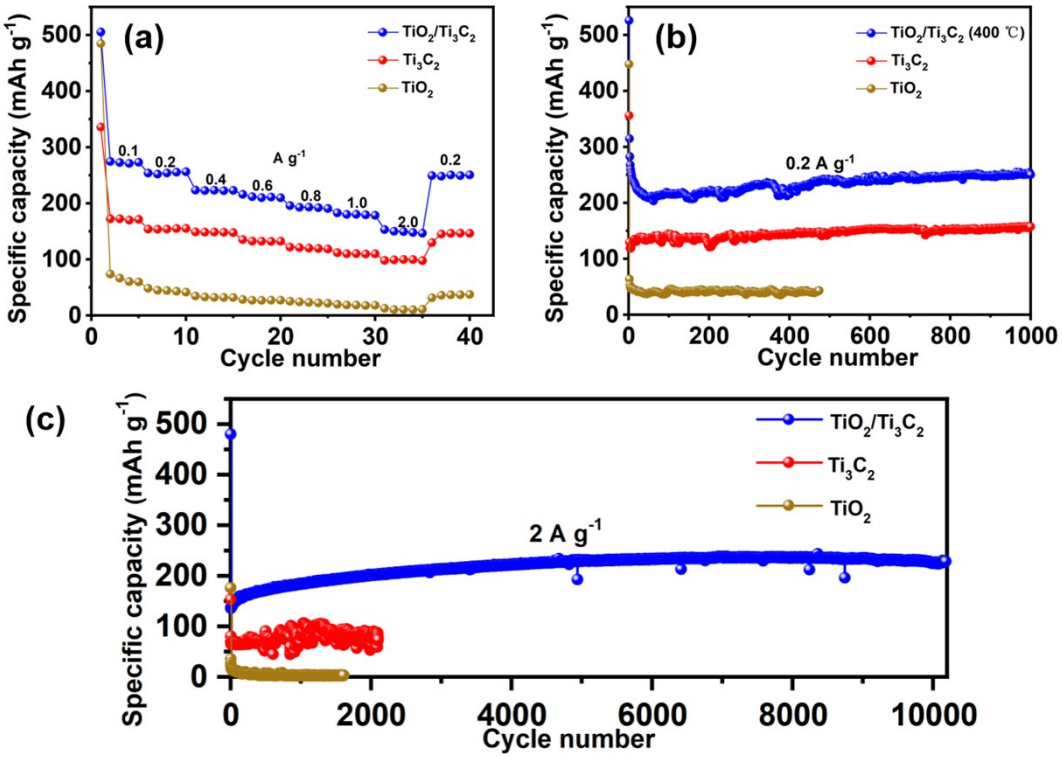

Figure S9. (a) Rate performance (b) Cycling stability at 0.2 A g^{-1} and (c) Long-term cycling performance at 2 A g^{-1} for TiO_2, Ti_3C_2 and TiO_2/Ti_3C_2 anodes.

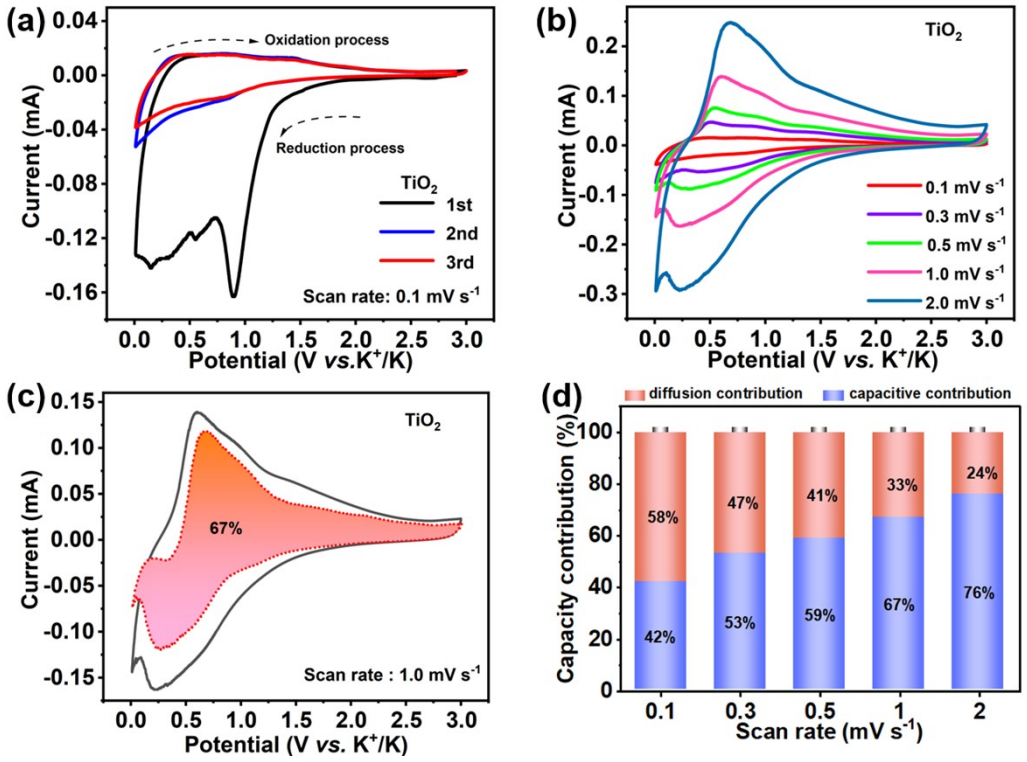

Figure S10. (a) The initial three CV curves at the scan rate of 0.1 mV s^{-1} (b) CV curves at various scan rates (c) Capacitive and diffusion-controlled contributions at 1.0 mV s^{-1} and (d) The contribution ratio of capacitive behaviors at different scan rates for the TiO_2 electrode.

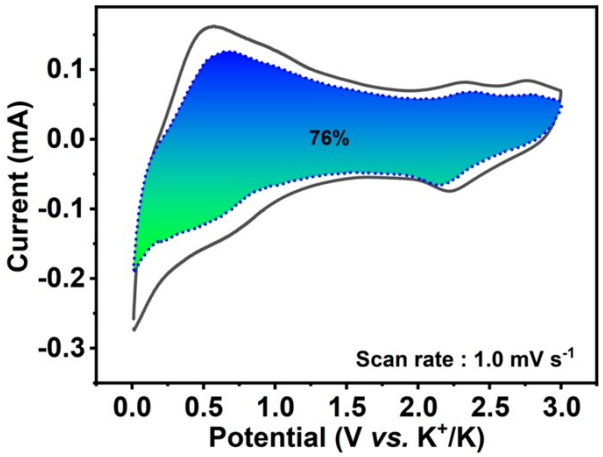

Figure S11. CV curve of capacitive contribution displayed by the filled pattern at the scan rate of 1.0 mV s^{-1} for Ti_3C_2.

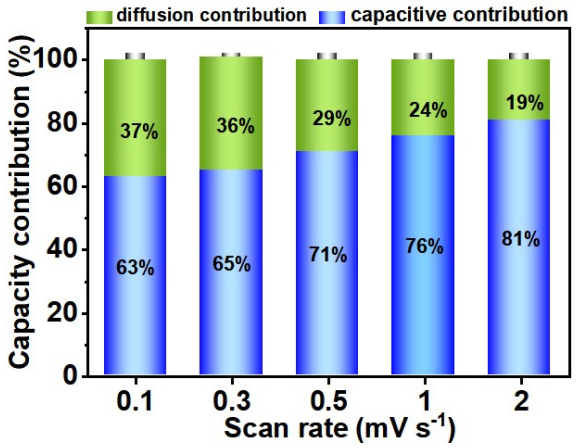

Figure S12. The contribution ratio of capacitive behaviors at different scan rates for Ti_3C_2.

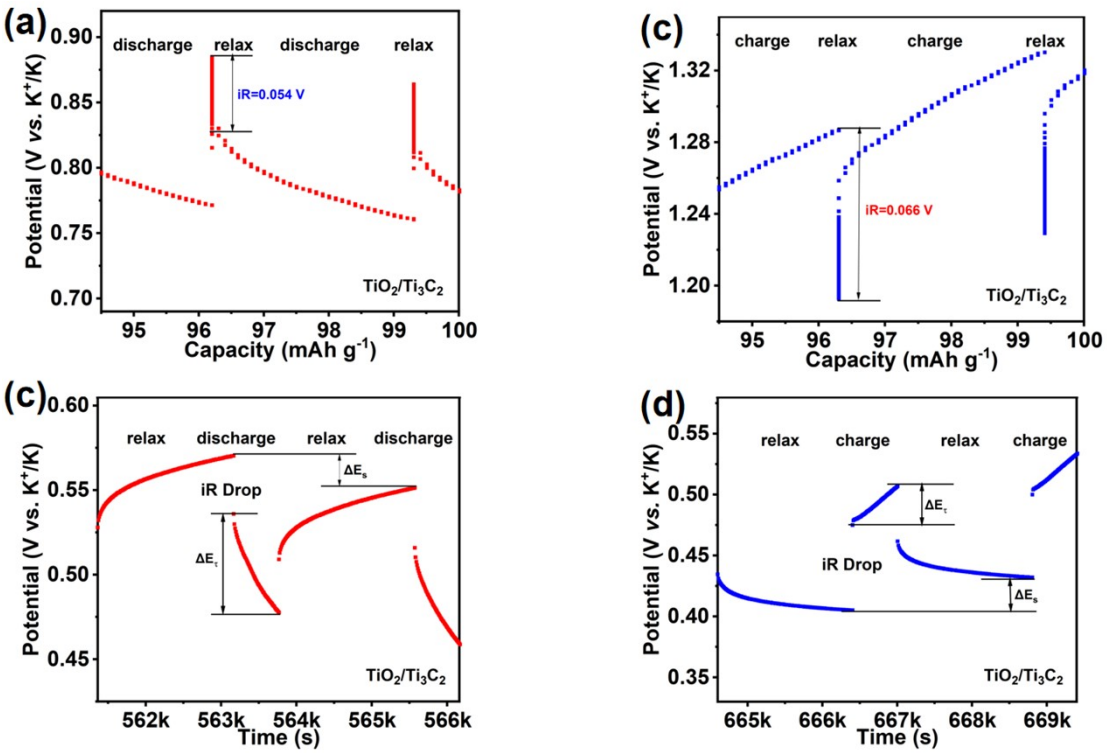

Figure S13. The magnified GITT profiles at process of (a) discharging and (b) charging. Schematic illustration of a typical single GITT step *vs.* time during (c) discharging and (d) charging.

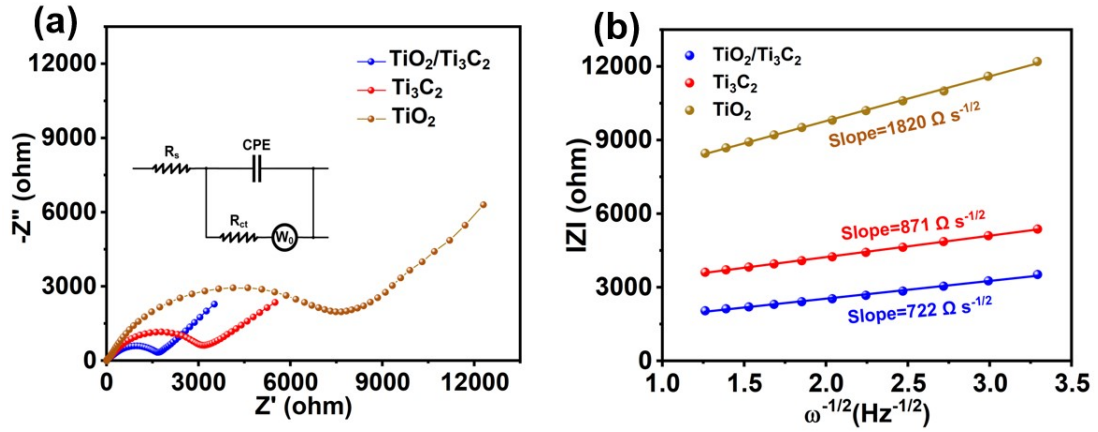

Figure S14. (a) The Nyquist plots and (b) Extracted |Z| versus $\omega^{-1/2}$ plots in the Warburg region for TiO_2, Ti_3C_2 and TiO_2/Ti_3C_2 electrodes.

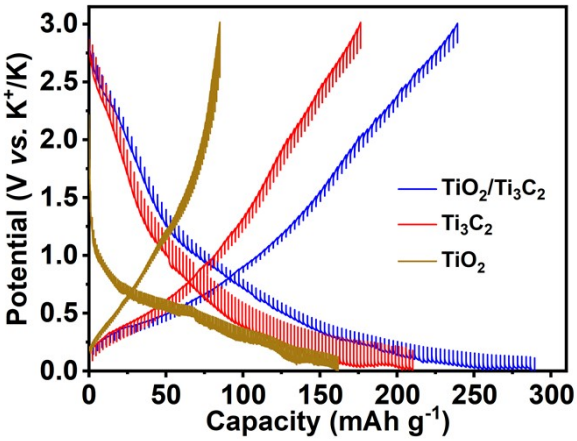

Figure S15. GITT profiles of TiO_2, Ti_3C_2 and TiO_2/Ti_3C_2 electrodes during potassiation/de-potassiation processes.

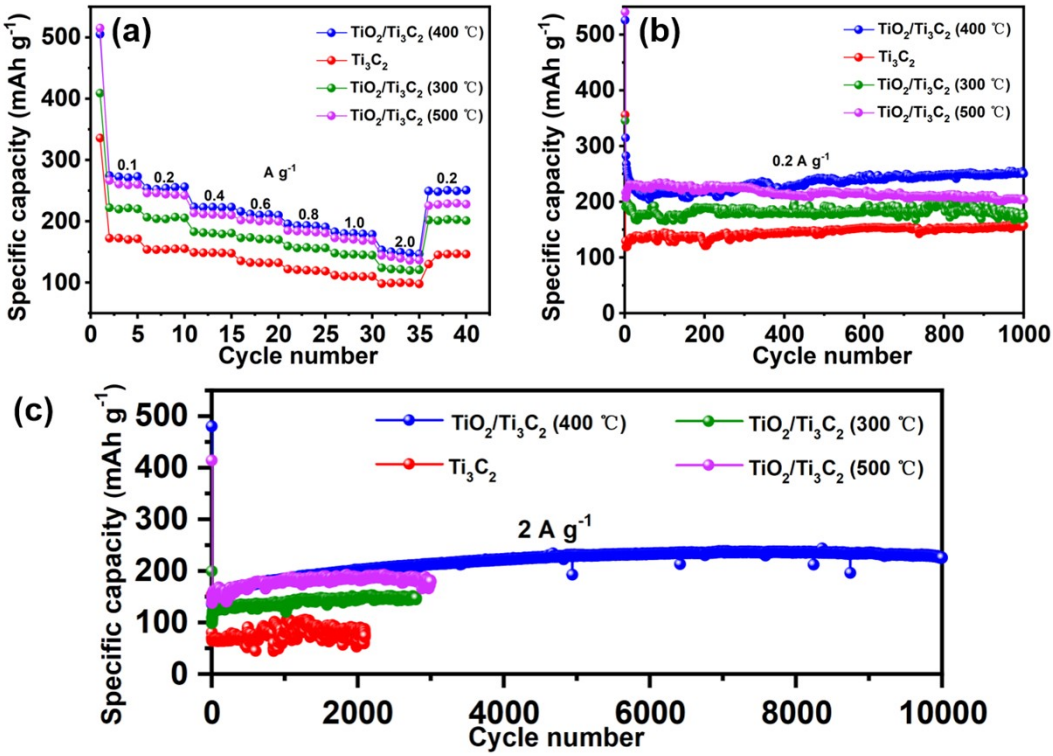

Figure S16. (a) Rate performance (b) Cycling stability at 0.2 A g^{-1} and (c) Long-term cycling performance at 2 A g^{-1} for Ti_3C_2 and TiO_2/Ti_3C_2 anodes at 300 ℃, 400 ℃ and 500 ℃.

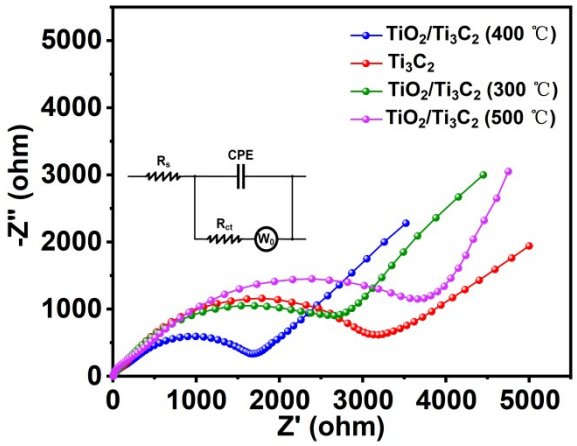

Figure S17. Nyquist plots of Ti_3C_2 and TiO_2/Ti_3C_2 electrodes at 300 ℃, 400 ℃, 500 ℃.

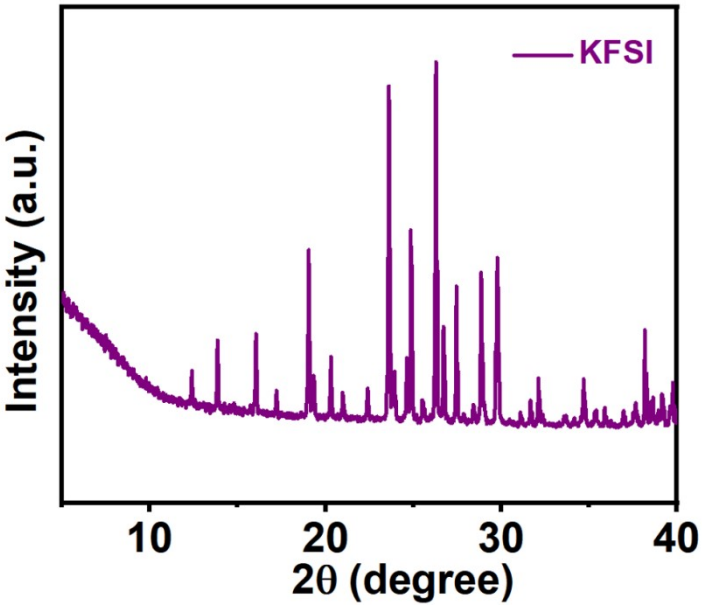

Figure S18. The XRD pattern of the potassium bis (fluorosulfonyl) imide (KFSI).

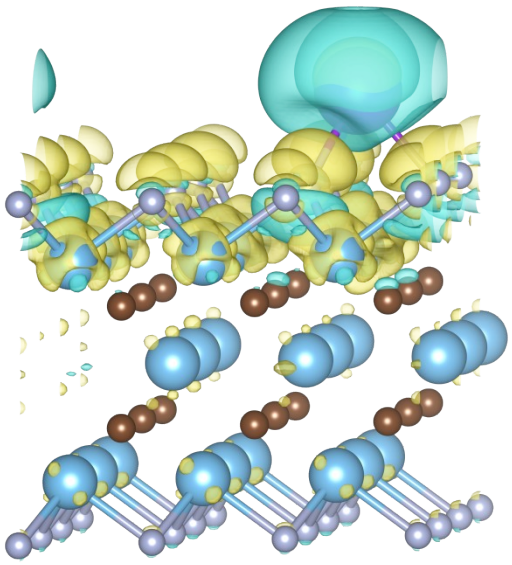

Figure S19. Calculated charge density differences for a single K adsorbed on the $Ti_3C_2F_2$ The yellow and blue colors represent charge accumulation and charge depletion, respectively.

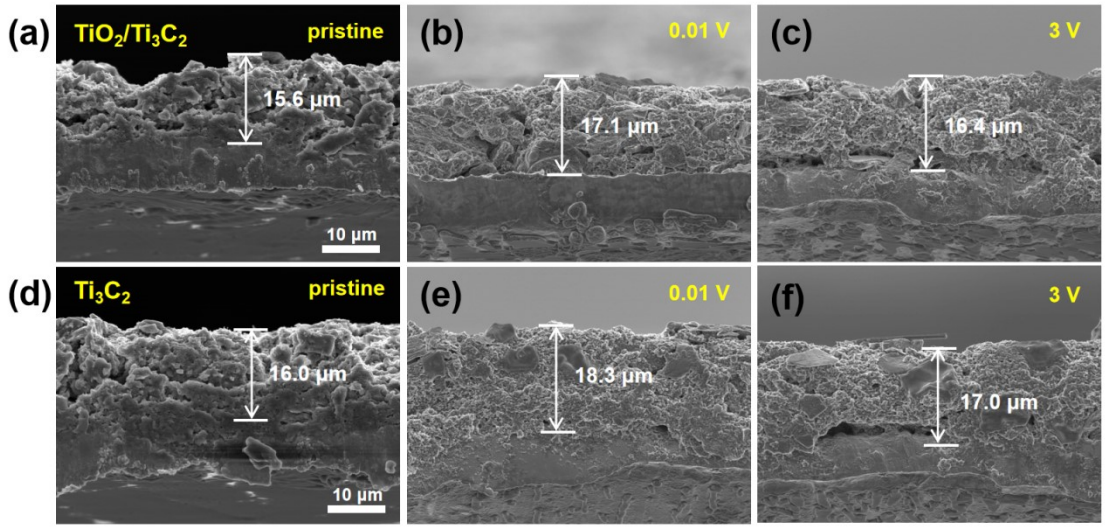

Figure S20. Cross-sectional SEM images of pristine, after-discharge, and after-charge of the initial cycle for TiO_2/Ti_3C_2 and Ti_3C_2 electrodes.

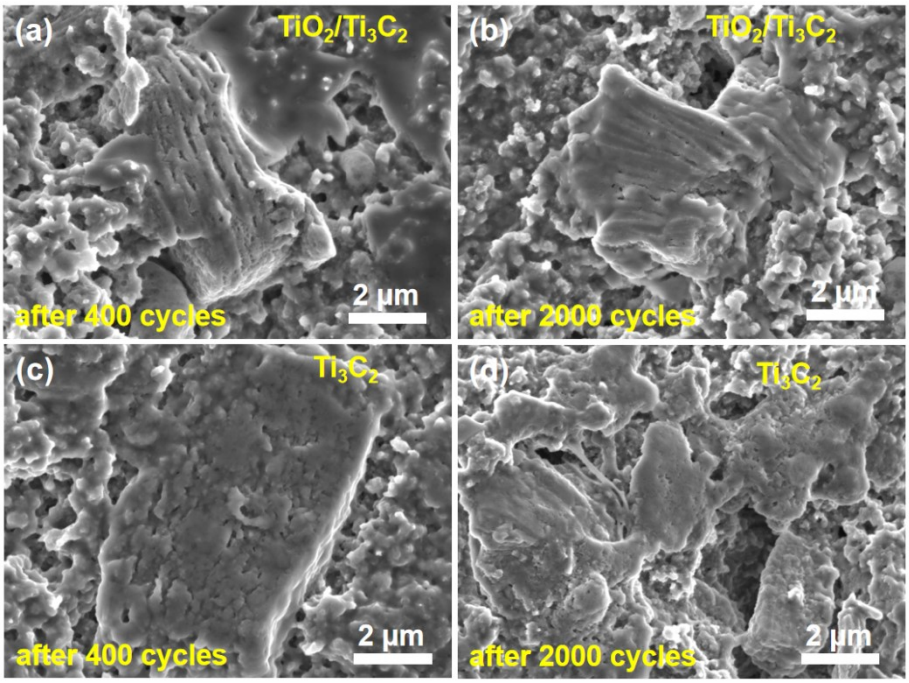

Figure S21. (a-d) SEM images of electrodes with their SEI after 400 and 2000 cycles for TiO_2/Ti_3C_2 and Ti_3C_2.

Table S1. Atomic percent summary of main elements obtained by XPS survey spectrum analysis for the Ti_3C_2 and TiO_2/Ti_3C_2 hybrid.

	Atomic (%)	
Element	**Ti_3C_2**	**TiO_2/Ti_3C_2**
Ti	14.71	8.95
C	49.63	53.91
O	19.93	32.56
F	15.74	4.57

Table S2. Summary of previously reported Ti_3C_2-based anode materials for alkali metal ion batteries application, and electrochemical performance.

Materials	Application	Rate capacity ($mAh\ g^{-1}$)	Cycle life	Reference

Alkalized Ti_3C_2 MXene nanoribbons	SIBs	85 mAh g^{-1} at 0.3 A g^{-1}	~50 mAh g^{-1} at 0.2 A g^{-1} after 500 cycles	7
	PIBs	60 mAh g^{-1} at 0.3 A g^{-1}	42 mAh g^{-1} at 0.2 A g^{-1} after 500 cycles	
Accordion-like $TiO_2/Ti3C_2$ nanohybrid	LIBs	149 mAh g-1 at 2 A g-1	~140 mAh g^{-1} at 2 A g^{-1} after 2000 cycles	8
	SIBs	52 mAh g^{-1} at 2 A g^{-1}	101 mAh g^{-1} at 0.2 A g^{-1} after 500 cycles	
Nitrogen-doped carbon decorated TiO_2/Ti_3C_2Tx MXene	SIBs	100 mAh g^{-1} at 10 A g^{-1}	158 mAh g^{-1} at 2 A g^{-1} after 1900 cycles	9
Nanoribbons of Na/K titanate (M-NTO/KTO)	SIBs	101 mAh g^{-1} at 2 A g^{-1}	~150 mAh g^{-1} at 0.2 A g^{-1} after 150 cycles	10
	PIBs	81 mAh g^{-1} at 0.3 A g^{-1}	~45 mAh g^{-1} at 0.2 A g^{-1} after 900 cycles	
$TiSe_2/TiO_2/C$ heterostructured hexagonal prisms	SIBs	212 mAh g^{-1} at 10 A g^{-1}	280 mAh g^{-1} at 5 A g^{-1} after 1000 cycles	11
	PIBs	~40 mAh g^{-1} at 5 A g^{-1}	121 mAh g^{-1} at 0.1 A g^{-1} after 800 cycles	
Pillar-free	SIBs	~152 mAh g^{-1}	153 mAh g^{-1}	12

TiO_2/Ti_3C_2 composite		at 1 A g^{-1}	at 0.6 A g^{-1} after 100 cycles	
$Ti_3C_2@Al_2O_3$ composites.	LIBs	~148 mAh g^{-1} at 2 A g^{-1}	~286 mAh g^{-1} at 1 A g^{-1} after 500 cycles	13
p-$Ti_3C_2T_x$ /CNT	LIBs	330 mAh g^{-1} at 3.2 A g^{-1}	~500 mAh g^{-1} at 0.16 A g^{-1} after 100 cycles	14
CT-S@Ti_3C_2-450	SIBs	120 mAh g^{-1} at 15 A g^{-1}	~75 mAh g^{-1} at 10 A g^{-1} after 5000 cycles	15
na-$Ti_3C_2T_x$	LIBs	58.2 mAh g^{-1} at 5 A g^{-1}	~106 mAh g^{-1} at 0.5 A g^{-1} after 500 cycles	16
Hierarchical TiO_2/Ti_3C_2 hybrid	PIBs	150 mAh g^{-1} at 2 A g^{-1}	~230 mAh g^{-1} at 2 A g^{-1} over 10000 cycles	**This work**

Reference

1 Perdew, Chevary, Vosko, Jackson, Pederson, Singh and Fiolhais, Atoms, molecules, solids, and surfaces: Applications of the generalized gradient approximation for exchange and correlation, *Physical review. B, Condensed matter*, 1992, **46**, 6671.

2 Kresse and Furthmuller, Efficient iterative schemes for ab initio total-energy calculations using a plane-wave basis set, *Physical review. B, Condensed matter*, 1996, **54**, 11169.

3 P. E. Blochl, C. J. Forst and J. Schimpl, Projector augmented wave method: ab initio molecular dynamics with full wave functions, *Bull. Mat. Sci.*, 2003, **26**, 33.

4 Perdew, Burke and Ernzerhof, Generalized Gradient Approximation Made Simple, *Physical review letters*, 1996, **77**, 3865.

5 Bader, Principle of stationary action and the definition of a proper open system, *Physical review. B, Condensed matter*, 1994, **49**, 13348.

6 S. Grimme, S. Ehrlich and L. Goerigk, Effect of the Damping Function in Dispersion Corrected Density Functional Theory, *Journal of Computational Chemistry*, 2011, **32**, 1456.

7 P. Lian, Y. Dong, Z.-S. Wu, S. Zheng, X. Wang, W. Sen, C. Sun, J. Qin, X. Shi and X. Bao, Alkalized Ti_3C_2 MXene nanoribbons with expanded interlayer spacing for high-capacity sodium and potassium ion batteries, *Nano Energy*, 2017, **40**, 1.

8 C. Yang, Y. Liu, X. Sun, Y. Zhang, L. Hou, Q. Zhang and C. Yuan, In-situ construction of hierarchical accordion-like TiO_2/Ti_3C_2 nanohybrid as anode material for lithium and sodium ion batteries, *Electrochimica Acta*, 2018, **271**, 165.

9 F. Wang, X. Ma, P. Zou, G. Wang, Y. Xiong, Y. Liu, F. Ren and X. Xiong, Nitrogen-doped carbon decorated TiO_2/Ti_3C_2T MXene composites as anode material for high-performance sodium-ion batteries, *Surface and Coatings Technology*, 2021, **422**, 127568.

10 Y. Dong, Z.-S. Wu, S. Zheng, X. Wang, J. Qin, S. Wang, X. Shi and X. Bao, Ti_3C_2 MXene-Derived Sodium/Potassium Titanate Nanoribbons for High-Performance Sodium/Potassium Ion Batteries with Enhanced Capacities, *ACS Nano*, 2017, **11**, 4792.

11 F. Qi, L. Shao, X. Lu, G. Liu, X. Shi and Z. Sun, MXene-derived $TiSe_2/TiO_2/C$ heterostructured hexagonal prisms as high-rate anodes for Na-ion and K-ion batteries, *Applied Surface Science*, 2022, **605**, 154653.

12 P. Wang, X. Lu, Y. Boyjoo, X. Wei, Y. Zhang, D. Guo, S. Sun and J. Liu, Pillar-free TiO_2/Ti_3C_2 composite with expanded interlayer spacing for high-capacity sodium ion batteries, *Journal of Power Sources*, 2020, **451**, 227756.

13 X. Hui, D. Zhao, P. Wang, H. Di, X. Ge, P. Zhang and L. Yin, Oxide Nanoclusters on Ti_3C_2 MXenes to Deactivate Defects for Enhanced Lithium Ion Storage Performance, *Small*, 2021, **18**, 2104439.

14 C. E. Ren, M. Q. Zhao, T. Makaryan, J. Halim, M. Boota, S. Kota, B. Anasori, M. W. Barsoum and Y. Gogotsi, Porous Two-Dimensional Transition Metal Carbide (MXene) Flakes for High-Performance Li-Ion Storage, *ChemElectroChem*, 2016, **3**, 689.

15 J. Luo, J. Zheng, J. Nai, C. Jin, H. Yuan, O. Sheng, Y. Liu, R. Fang, W. Zhang, H. Huang, Y. Gan, Y. Xia, C. Liang, J. Zhang, W. Li and X. Tao, Atomic Sulfur Covalently Engineered Interlayers of Ti_3C_2 MXene for Ultra-Fast Sodium-Ion Storage by Enhanced Pseudocapacitance, *Advanced Functional Materials*, 2019, **29**, 1808107.

16 L. Huang, T. Li, Q. Liu and J. Gu, Fluorine-free $Ti_3C_2T_x$ as anode materials for Li-ion batteries, *Electrochemistry Communications*, 2019, **104**,106472.